Acta Oceanol. Sin., 2026, Vol. 45, No. 2, P. 1–13
https://doi.org/10.1007/s13131-025-2587-9

Multi-method characterization of grain-size sensitive components in deep-sea sediments from the Zhongnan Seamount, South China Sea: implications for monsoon-volcanic interactions and turbidity current events

Yuanfu Yue[1*†], Xintian Yu[1†], Liuying He[1†], Xinmeng Yuan[1], Kefu Yu[1, 2*]

[1] Guangxi Laboratory on the Study of Coral Reefs in the South China Sea, Coral Reef Research Centre, School of Marine Sciences, Guangxi University, Nanning 530004, China

[2] Southern Marine Science and Engineering Guangdong Laboratory (Zhuhai), Zhuhai 519080, China

Received 11 July 2025; accepted 14 December 2025

Abstract

Grain-size sensitive component separation (GSCS) methods are pivotal for paleoenvironmental reconstruction but remain underexplored in tectonically active deep-sea seamount settings like the central South China Sea (SCS).This study presents the first systematic comparison of three GSCS techniques, namely standard deviation (STD), end-member modeling (EMM), and principal component analysis (PCA). These methods are applied specifically to sediment core GT-06 recovered from the Zhongnan Seamount in the central South China Sea. By integrating grain-size unmixing with complementary proxies, including magnetic susceptibility (MS) and loss on ignition (LOI), we assess the resolving power of each method and relate the resulting components to site-specific sedimentary processes (e.g., summer monsoon, volcanic activity, seamount collapse-induced turbidity currents). Key results show that all methods identified three dominant grain-size ranges (clay, silt-sand, coarse sand) with robust inter-method correlations. Critically, EMM and PCA uniquely resolved a volcanic-derived silt component (EM2) that was undetectable using the STD method, highlighting a key limitation of STD in complex settings. Four geologically meaningful end-members were identified: (1) fine-grained terrigenous clay linked to the East Asian summer monsoon (EASM), (2) volcanic detritus reflecting Quaternary submarine eruptions, (3) siliceous biogenic debris indicative of monsoon-modulated productivity, and (4) coarse calcareous fragments associated with seamount collapse-induced turbidity currents. The results highlight the superior ability of EMM/PCA to resolve complex signals, whereas STD serves as an efficient yet limited tool for first-order screening. Together, these methods form a site-adapted framework for tectonically active deep-sea seamounts: EMM/PCA enabling fine-scale interpretation of monsoon-volcanic-turbidity interactions, and STD supports rapid large-dataset comparison. This workflow improves the reliability of paleoenvironmental reconstructions in mixed-signal settings like the Zhongnan Seamount.

Key words grain-size sensitive component separation, South China Sea, Zhongnan Seamount, East Asian monsoon, volcanic activity, turbidity currents, deep-sea sediments

Citation Yue Yuanfu, Yu Xintian, He Liuying, Yuan Xinmeng, Yu Kefu. 2026. Multi-method characterization of grain-size sensitive components in deep-sea sediments from the Zhongnan Seamount, South China Sea: implications for monsoon-volcanic interactions and turbidity current events. Acta Oceanologica Sinica, 45(2): 1–13, doi: 10.1007/s13131-025-2587-9

Foundation item: The Guangxi Scientific Projects under contract No. 2025GXNSFAA069160; the Guangxi Science and Technology Program under contract No. AD25069075; the National Natural Science Foundation of China under contract No. 42366002; the Southern Marine Science and Engineering Guangdong Laboratory (Zhuhai) Program under contract Nos SML2021SI1004, SML2023SP215, SML2023SP218, and SML2023SP238; the NSFC Shiptime Sharing Project under contract Nos 42349911, 42449910, and 42449911.

*Corresponding author, E-mail: yuanfu.yue@gxu.edu.cn; kefuyu@scsio.ac.cn
†These authors contributed equally to this work.

1 Introduction

In Quaternary paleoenvironmental reconstruction, sediment grain-size is a key proxy for deciphering geological archives in marine settings, as these archives preserve critical information about sediment provenance, transport processes, and depositional dynamics (Yu et al., 2016). This is particularly true for deep-sea sediments in tectonically active marginal seas like the South China Sea (SCS, Fig. 1a). However, grain-size distributions typically reflect a complex mixture of multiple sources (e.g., terrigenous input, volcanic ash, and biogenic debris), and dynamic processes (e.g., turbidity currents and bottom-current sorting). Such complexity leads to overlapping signals from diverse depositional environments, making it challenging to isolate individual environmental drivers (Flemming, 2007; Weltje and Prins, 2003).

Traditional grain-size analysis methods, such as bulk parameter calculation (e.g., mean grain-size, sorting) and C-M plots (Zhao et al., 2017), struggle to resolve these mixed signals, especially in deep-sea settings. For instance, bulk grain-size parameters fail to distinguish terrigenous clay (transported by monsoonal rivers) from volcanic silt (derived from submarine eruptions) in the SCS central basin, as their hydrodynamic transport signatures overlap under weak deep-sea currents. Similarly, C-M plots often produce ambiguous results in settings with variable sediment supply, further limiting their use for high-resolution paleoenvironmental reconstructions.

Grain-size sensitive component separation (GSCS) methods address this limitation by decomposing complex distributions into discrete components, each linked to specific environmental drivers, directly overcoming the inability of traditional methods to resolve mixed signals (Weltje and Prins, 2003). Three widely used GSCS techniques, for instance, standard deviation (STD) (e.g., Boulay et al., 2003, marine adaptation), end-member modeling (EMM) (e.g., Boulay et al., 2007, Prins et al., 2000, for sediment application; Weltje, 1997, original framework), and principal component analysis (PCA) (e.g., Yi et al., 2012, marine adaptation) have advanced sedimentary research. Specifically, STD identifies grain-size intervals sensitive to environmental changes by quantifying variance in fractional abundances, with prior applications including detecting winter coastal current signals in continental shelf sediments (core S20, Tian et al., 2015); however, its effectiveness in deep-sea settings, where hydrodynamic conditions and sediment sources differ drastically from shallow waters, has not been systematically validated. EMM, based on non-negative matrix factorization, extracts genetically distinct end-members (Weltje and Prins, 2003). For example, EMM applied to northern SCS core PC338 successfully isolated a 2–10 μm terrigenous clay component (tied to summer monsoon intensity), signals unresolvable by traditional bulk parameters (Li et al., 2019). PCA reduces dimensionality to extract orthogonal principal components, with marine-adapted protocols (Yi et al., 2012) enabling separation of overlapping depositional signals in shelf and slope environments.

Although these GSCS methods have been widely applied in diverse marine settings spanning continental shelves to deep-sea basins (Chen et al., 2022; Jiang et al., 2023; Lin et al., 2023), their application in tectonically active deep-sea basins (e.g., the central SCS) remains underexplored. In such regions, sedimentary signals are uniquely shaped by overlapping processes: monsoon-driven terrigenous transport, submarine volcanic input, and seamount collapse-induced turbidity currents (Cai et al., 2018; Zhang et al., 2003). This complexity highlights the need to compare GSCS methods, as their ability to disentangle mixed sources and processes directly impacts the reliability of paleoenvironmental reconstructions.

The SCS (Fig. 1a), a semi-enclosed basin at the convergence of the Eurasian, Pacific, and Indo-Australian

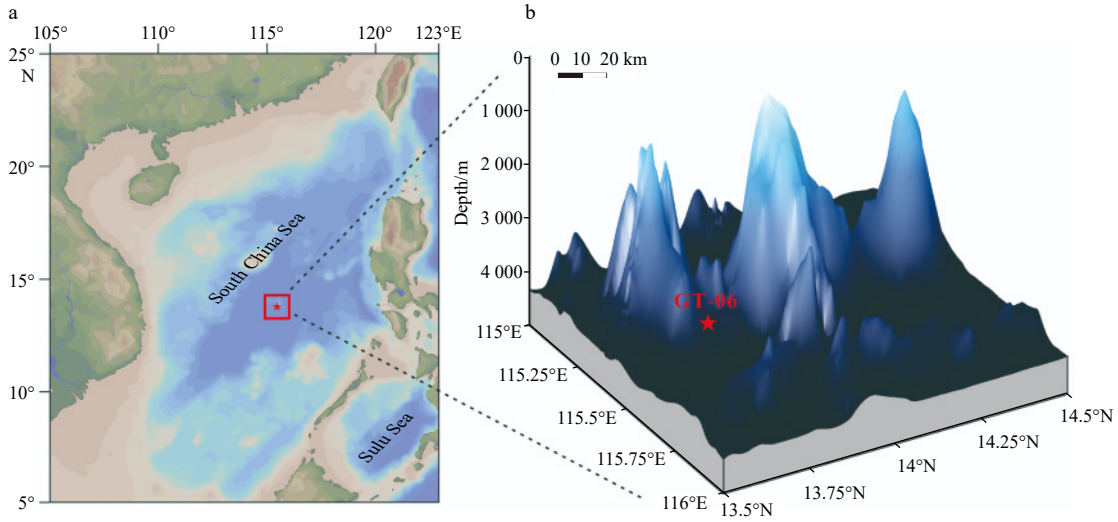

Fig. 1. The location and surrounding topography of the core GT-06(a), topography of the sampling area (b). Red star denotes core GT-06; black lines outline Zhongnan Seamount.

Plates, is a globally significant site for studying sedimentary responses to tectonic and climatic interactions (Wang, 2020; Yang et al., 2007). Its central basin (average water depth ~4 700 m) is uniquely challenging for sedimentary signal interpretation: it is dominated by seamounts and characterized by mixed provenances (monsoon-transported terrigenous material from the Red/Zhujiang Rivers, volcanic detritus from Luzon Arc, and biogenic debris; Cai et al., 2018, 2024; Zeng et al., 2025) and dynamic processes (e.g., turbidity currents triggered by seamount collapse or earthquakes; Zhang et al., 2003).

Among these seamounts, Zhongnan Seamount (13.81°N, 115.37°E, Fig. 1b) stands out as a key site for GSCS validation. Located at the structural boundary between the eastern and southwestern sub-basins of the central SCS, it captures overlapping signals: long-range terrigenous inputs (via monsoonal currents) and local volcanic detritus (from submarine eruptions). Critically, its water depth (~3 837 m) lies just below the carbonate compensation depth (CCD, ~3 400–4 000 m; Liu et al., 2022a; Wang and Chen, 2013), where deep-sea currents and carbonate dissolution further obscure mixed provenance signals (Cai et al., 2018). This setting not only amplifies the need for robust GSCS methods but also provides a natural "testbed" for resolving monsoon-volcanic-deep-sea dynamic interactions.

Notably, most previous GSCS studies in the SCS have focused on marginal slopes or continental shelves (e.g., Li et al., 2019; Yang et al., 2007). These studies rely on a limited number of methods (typically one or two, e.g., EMM, STD, or PCA) to interpret relatively simple sedimentary signals. In contrast, the deep sea environment of the central basin, which is featured with overlapping tectonic, climatic and oceanographic processes, has received little attention. This leaves a critical gap: how to reliably apply and compare multiple GSCS methods to separate complex signals in such settings.

Beyond grain-size-based proxies, other paleoenvironmental archives in the northern SCS, such as coral records, have also provided valuable insights into Holocene climate and sea-level dynamics. For instance, Yue et al. (2024) reconstructed Mid-Holocene sea-level highstands and corresponding climate responses in the northern SCS using coral records, confirming that monsoon variability during this period significantly modulated regional sedimentary processes. However, such high resolution climate sea level linkages remain understudied in the deep sea seamount settings of the central SCS. In these settings, tectonic and volcanic activities further complicate sedimentary signals, which emphasizes the value of our multimethod GSCS approach for separating mixed environmental drivers.

Given the tectonic-climatic-oceanographic complexity of the SCS central basin, which heightens the need for robust GSCS validation, we address two critical questions: (1) How do STD, EMM, and PCA differ in resolving mixed grain-size signals (e.g., monsoon-transported clays vs. volcanic ash) in the tectonically active SCS central basin? (2) Can integrating these three GSCS techniques with independent proxies [magnetic susceptibility (MS), loss on ignition (LOI)] improve the accuracy of paleoenvironmental proxies for interpreting both background depositional processes (e.g., biogenic productivity and hemipelagic sedimentation) and high-energy events (e.g., seamount collapse-induced turbidity currents)?

These questions address two longstanding gaps in SCS sedimentary research. First most previous GSCS studies have focus on marginal slopes or shelves, and no systematic comparison of STD, EMM, and PCA has been conducted in the tectonically active deep-sea of the central basin; Second Environmental interpretation of grain-size components, such as distinguishing volcanic from terrigenous sources, depends largely on regional analogies without site-specific evidence.

To address these gaps, we focus on core GT-06 collected from the Zhongnan Seamount in the central South China Sea. This site is uniquely suited to record mixed environmental signals. We combine GSCS with MS and LOI to achieve three main objectives. First, we assess the performance of STD, EMM, and PCA in deep sea environments. Second, we link grain size components to corresponding environmental processes. Third, we establish a multi-method GSCS protocol for complex marginal sea setting.

By analyzing core GT-06's unique sedimentary archive, this study resolves how tectonic, climatic, and oceanographic processes shape deep-sea sediments in the SCS. It also provides a transferable framework for similar tectonically active marginal seas (e.g., Caribbean, Mediterranean), where overlapping processes demand advanced multi-technique approaches.

2 Study area

The Zhongnan Seamount (13.81° N, 115.37° E; Fig. 1b) is situated at the structural boundary between the eastern and southwestern sub-basins of the SCS, within a tectonically active zone shaped by multi-plate convergence (Wang, 2020). Geographically, the Zhongnan Seamount occupies the northeastern margin of the southwest sub-basin, forming a prominent volcanic edifice that rises approximately 3 600 m above the adjacent seafloor. Its morphology is characterized by a gently dipping northern slope and a steep southern flank. Basalt recovered from the northern slope yields an Ar-Ar age of (6.64 ± 0.42) Ma, indicating that the seamount was constructed during the late Miocene phase of seafloor spreading in the SCS (Yan et al., 2014; Zeng et al., 2025).

This location makes it ideal for validating GSCS methods, as its flanks capture three key sedimentary signals critical for testing method resolution: (1) Long-range terrigenous input: Fine silt/clay (grain-size ⩽63 μm) transported ~1 000 km from the Red/Zhujiang Rivers via monsoonal currents (Cai et al., 2024; Zeng et al., 2025);

(2) Local volcanic detritus: Quaternary submarine eruptions from the Luzon Arc, transported to the seamount via deep-sea turbidity currents (~17 Ma; Wang et al., 2024; Cai et al., 2018, 2022); and (3) Episodic turbidity currents: triggered by seamount collapse, depositing coarse calcareous debris (Howe et al., 2006).

Core GT-06 was recovered from the southern flank of Zhongnan Seamount at a water depth of 3 837 m (Fig. 1b), which is just below the SCS CCD (~3 400–4 000 m). While the central basin (average water depth about 4 700 m) is dominated by intense carbonate dissolution, the seamount flank acts as a localized "topographic high-stand". Here, bottom currents slow down, which mitigating dissolution and facilitates the preservation of calcareous bioclasts (e.g., foraminiferal tests) in episodic turbidity deposits (Cai et al., 2018; Zhang et al., 2003). This is a critical feature for studying high-energy events in deep-sea settings and testing GSCS method accuracy.

3 Materials and methods

3.1 *Sampling collection and stratification*

Core GT-06 (total length: 517 cm) was collected from the southern flank of Zhongnan Seamount (13.812 4°N, 115.374 6°E; 3 837 m water depth) in the central SCS (Fig. 1b), with undisturbed sediment recovery confirmed by visual inspection of lithological continuity (e.g., no internal deformation of the carbonate-rich A1 layer, 50–58 cm).

A lithology-guided stratified sampling strategy was adopted to reflect the core's depositional characteristics: top 10 cm: 2-cm intervals (5 samples) to capture high-resolution signals of short-lived events (e.g., turbidity current fluctuations); remaining 507 cm (10–517 cm): 4-cm intervals (125 samples) to resolve long-term background sedimentation. In total, 130 samples were obtained for multi-proxy analyses, including grain-size, MS, and LOI.

3.2 *Laboratory analyses*

All analyses were conducted in Guangxi Laboratory on the Study of Coral Reefs in the South China Sea, Guangxi University, with strict quality control (e.g., blank samples, triplicate measurements) to ensure data reliability.

3.2.1 *Grain-size analysis (including GSCS techniques)*

Laser diffraction measurement: Grain-size distribution was determined using a Malvern Mastersizer 3000 [measurement range: 0.01–3 500 μm; resolution: ϕ0.01, $\phi = -\log_2(d/d_0)$]. Each sample was measured in triplicate, yielding a relative standard deviation (RSD) of <3% (calculated from triplicate mean grain-size values) to ensure reproducibility. Grain-size parameters [mean grain-size (Mz), median diameter (Md), sorting coefficient (σ_1), skewness (Sk_1), kurtosis (Kg)] were calculated via the Folk-Ward graphical method (Folk and Ward, 1957).

Grain-size sensitive component separation (GSCS): Three techniques were applied to decompose mixed grain-size signals, with key parameters optimized to match the deep-sea sedimentary characteristics of core GT-06. We selected these methods to leverage their complementary strengths: EMM for defining physically meaningful end-members, PCA for extracting variance-based components, and STD for its computational efficiency in rapid screening.

PCA was conducted in SPSS 26 using volume- normalized grain-size data (1-phi intervals, 0.01–3 500 μm). Varimax rotation was applied to extract orthogonal components with eigenvalues >1, ensuring a cumulative variance exceeding 90%.

EMM is implemented in MATLAB 2021b using the AnalySize toolbox (Paterson and Heslop, 2015). Non-negative matrix factorization was applied, with the optimal number of end-members determined by two criteria: (1) reconstruction variance >99.6% (minimizing data fitting error) and (2) average angular deviation <5° (ensuring end-member distinctiveness; Prins et al., 2000).

The STD method was implemented in Python to identify grain-size intervals with high sensitivity, calculated at 0.1-phi intervals over the range 0.01–3 500 μm. Sensitive grain-size intervals were identified as the modes corresponding to relatively high STD values, following Boulay et al. (2003).

3.2.2 *Magnetic susceptibility (MS) and loss on ignition (LOI)*

MS was measured using a Bartington MS2 meter with an MS2F sensor (resolution: 1×10^{-8} SI), calibrated to zero before each measurement and averaged over three readings to minimize noise. MS data were used to verify volcanic detritus (high MS values indicate abundant magnetic minerals in volcanic particles; Chen et al., 2007; Shin et al., 2020).

LOI was determined to quantify organic matter (LOI550, burned at 550℃) and carbonate (LOI950, burned at 950℃) contents. Samples were first weighed (W_1) and then heated at 105℃ for 24 hours to constant weight (W_2, to remove moisture); then sequentially heated at 550℃ for 4 hours (to oxidize OM) and weighed (W_3); LOI550 = $[(W_2 - W_3)/W_2] \times 100\%$ (OM content); finally, samples were heated at 950℃ for 2 hours (to decompose $CaCO_3$) and weighed (W_4); LOI950 = $[(W_3 - W_4)/W_2] \times 100\%$ ($CaCO_3$ content).

Each measurement included three replicate samples and one standard reference material (soil CRM GBW07401), with LOI RSD <5% and CRM recovery rate 95%–105% (quality control criteria). LOI550 was used to validate biogenic productivity, while LOI950 indicated turbidity current events (high $CaCO_3$ preservation).

Pearson correlation coefficients (r) were calculated to assess relationships between grain-size sensitive components and environmental proxies (MS, LOI).

4 Result

4.1 *Lithological unit and basic characteristics of grain-size data*

Grain-size analysis of core GT-06 yields the following key bulk parameters (Fig. 2), which form the basis for subsequent GSCS and lithological validation.

The sediment is predominantly composed of silt (21.86%–81.74%, mean 69.52%), followed by sand (8.01%–76.16%, mean 22.36%) and clay (1.99%–14.06%, mean 8.12%). As shown in Fig. 2, the Mz ranges from ϕ2.76 to ϕ6.95 and Md varies between ϕ1.23 and ϕ6.87 (mean ϕ4.05), with overall poor sorting (sorting coefficient σ_1: ϕ1.82–ϕ3.53, mean ϕ2.37), variable skewness (Sk_1: ϕ−0.71 to ϕ0.51), and kurtosis (Kg: ϕ0.64–ϕ1.31).

Lithological units are further validated by grain-size parameters and geochemical proxies (LOI, MS; Fig. 2):

Unit A (0–142 cm) is characterized by coarser Mz (ϕ2.76–ϕ6.06) and higher organic matter content (LOI550: 8.18%–14.96%, mean 11.45%). A distinct carbonate-rich subunit (A1, 50–58 cm) within Unit A has a LOI950 of 28.34%, far exceeding the central SCS basin average (<4%, Cai et al., 2022), and exhibits the coarsest Mz (ϕ2.76–ϕ4.47) and very poor sorting (σ_1: ϕ2.32–ϕ2.85) in the core. Based on these textural and compositional anomalies, specifically the abrupt coarsening and high carbonate content, we explicitly interpret subunit A1 as a turbidite deposit.

Unit B (142–510 cm) is finer-grained than Unit A (Mz: ϕ4.22–ϕ6.95) with lower organic matter (LOI550: 5.24%–16.46%, mean 8.87%) and carbonate (LOI950: 1.50%–8.13%, mean 3.74%). Periodic LOI550 peaks (e.g., 234–314 cm, Fig. 2) correlate with slightly coarser Mz (~ϕ4.21–ϕ6.69).

The bulk grain-size distribution curves (Fig. 3) show multimodal patterns (2–3 dominant peaks) with consistent characteristics within each unit: Units A and B both show a fine-grained peak (~3–6 μm) and a medium-grained peak (~20–50 μm/50–90 μm). As shown in Fig. 3, Unit B exhibits a broad coarse-grained peak (~300–600 μm, sand), which is predominantly absent in the main body of Unit A. However, subunit A1 displays a distinct curve cluster, with the coarse-grained peak (~350 μm) significantly enhanced (relative abundance >16.21%) compared to other parts of Unit A (~0–4.73%).

4.2 *Results of grain-size sensitive component separation (GSCS)*

4.2.1 *Principal Component Analysis (PCA)*

PCA extracted 5 components with eigenvalues >1 (cumulative variance 98.2%, Table S1) with F5 excluded due to negligible variance contribution (<3.2%).

The rotated factor loading matrix identifies four grain-size components (Fig. 4). In this context, high factor loadings signify specific grain-size intervals that covary strongly, thereby isolating distinct sedimentary populations controlled by specific transport or depositional mechanisms.

F1 explains the largest variance (32.5%) and is dominated by the clay range (0.4–1.5 μm);

F2 (23.9%) and F4 (15.4%) represent the medium silt (27.4–51.8 μm) and coarse silt–fine sand (98.1–143.9 μm) fractions, respectively;

Notably, F3 (23.3%) exhibits dual loading peaks, distinguishing fine silt (F3-1: 8.7–14.5 μm) and coarse sand with negative loading (F3-2: 309.5–515.8 μm).

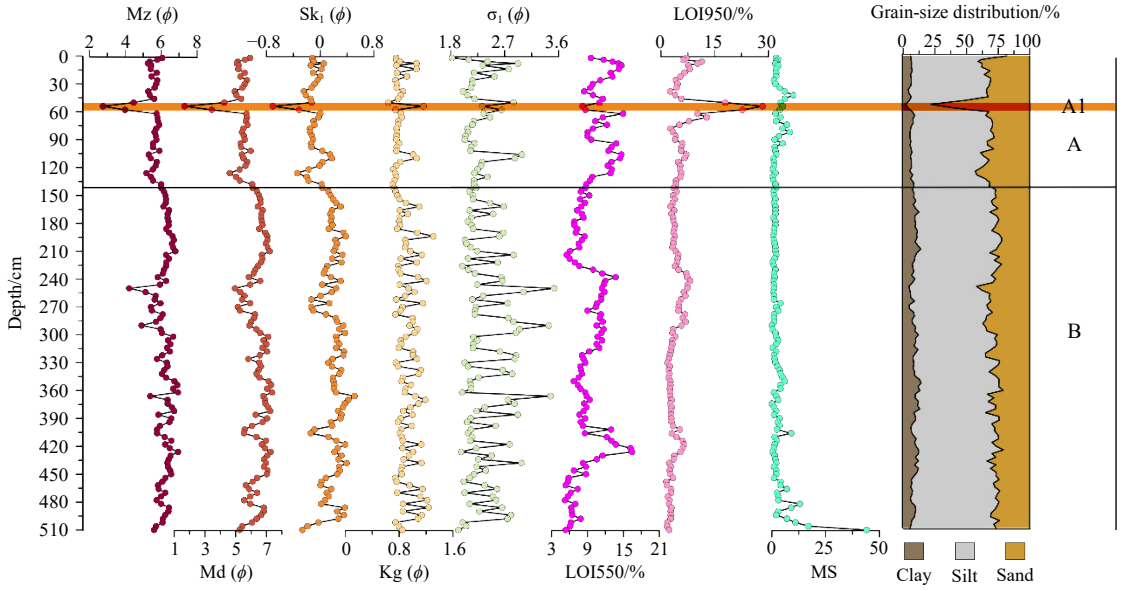

Fig. 2. Vertical variations of grain-size parameters, LOI and MS in core GT-06. Lithological units are delineated by a horizontal line at 142 cm (Unit A: 0–142 cm; Unit B: 142–510 cm); Orange-red shading marks subunit A1 (50–58 cm, high carbonate content). Abbreviations: Mz (mean grain-size), Md (median diameter), σ_1 (sorting coefficient), Sk_1 (skewness), Kg (kurtosis), LOI550 (organic matter content), LOI950 (carbonate content), MS (magnetic susceptibility). [$\phi = -\log_2(d/d_0)$].

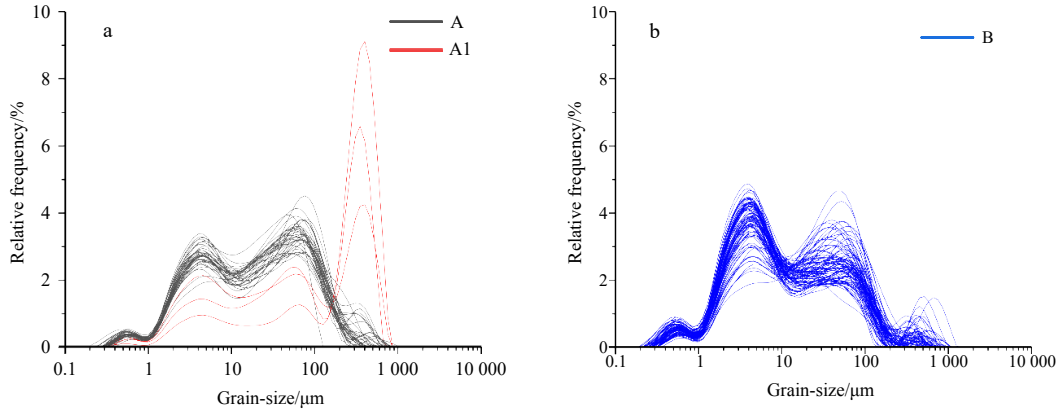

Fig. 3. Grain-size characteristics of core GT-06. a. Grain-size distribution curves of Unit A (0–142 cm), with the red lines highlighting subunit A1 (50–58 cm); b. grain-size distribution curves of Unit B (142–510 cm)

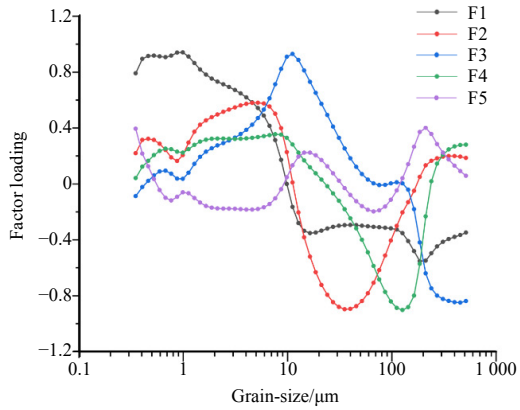

Fig. 4. PCA results for core GT-06, showing factor loadings across grain-size classes.

4.2.2 *End-member modeling (EMM)*

EMM was performed via non-negative matrix factorization (AnalySize, MATLAB 2021b). The optimal number of end-members was determined by two metrics (Figs 5a and b): (1) reconstruction variance stabilized at 99.6% and (2) average angular deviation decreased to <5° (indicating distinct end-member signals).

Four end-members with distinct modal peaks were extracted (Fig. 5c):

EM1 represents a fine-grained component with a modal peak at 4.0 μm (range: 2.1–6.7 μm) and an average abundance of 38.2%;

EM2 corresponds to a medium silt component, peaking at 35.3 μm (range: 27.4–45.6 μm), with an overall average abundance of 28.8%;

EM3 is identified as a coarse silt–fine sand component, peaking at 86.4 μm (range: 58.9–98.1 μm), accounting for 28.9% of total abundance;

Finally, EM4 denotes a coarse sand component, with a modal peak at 351.7 μm (range: 309.5–453.9 μm) and low average abundance (4.1%).

4.2.3 *Grain-size standard deviation (STD) method*

STD was calculated for 0.1-phi intervals to identify sensitive grain-size intervals (Fig. 6). Three distinct peaks were observed, with the following characteristics:

S1: Fine clay interval (2.8–4.6 μm) with a modal peak at 4.0 μm, and an average STD of 0.73;

S2: Medium silt–fine sand interval (58.9–86.3 μm), peaking at 86.3 μm, with an average STD of 0.67;

S3: Coarse sand interval (309.5–453.9 μm), peaking at 400.0 μm, and exhibiting the highest average STD (1.03) among all intervals.

The delineation of these intervals relies on visual identification and lacks a universal statistical criterion (reflecting an inherent subjectivity in the method), S1, S2, and S3 nonetheless show substantial overlap with the grain-size ranges of EM1, EM3, and EM4, respectively. In contrast,

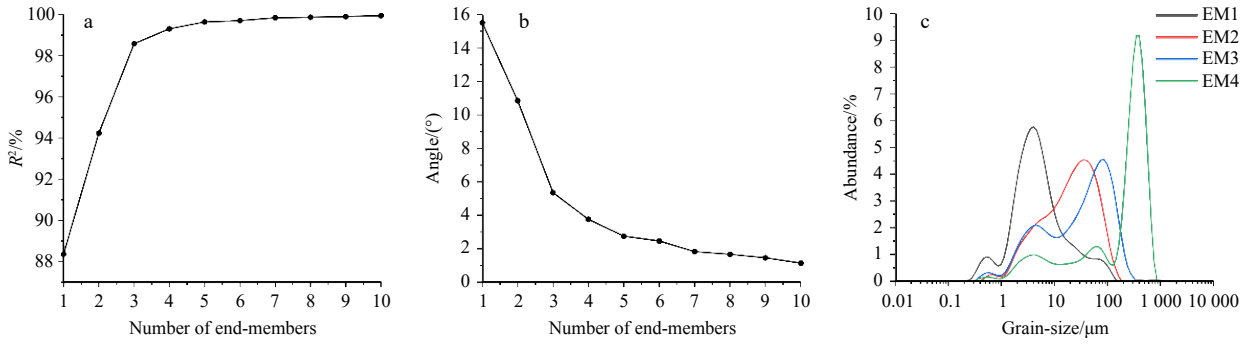

Fig. 5. Grain-size end-member analysis results: a. Model fit (R^2) vs. number of end-members; b. average angular deviation; c. grain-size frequency curves for four end-members, with modal peaks at (EM1: 4.0 μm, EM2: 35.3 μm, EM3: 86.4 μm, EM4: 351.7 μm).

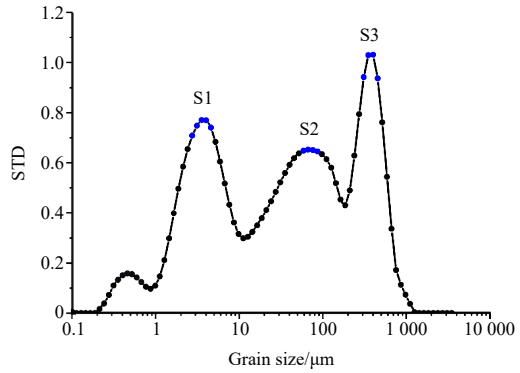

Fig. 6. Grain-size standard deviation (STD) analysis in core GT-06 sediments, highlighting three sensitive intervals (S1–S3).

EM2 (27.4–45.6 μm) lacks a corresponding STD peak, attributed to its low abundance (<5% in most samples) and partial overlap with EM3 on grain-size distribution curves (Section 5.1.1). These results highlight that while STD serves as a rapid screening tool, it has limitations in resolving complex signals compared to multivariate methods. This comparison thus provides a foundation for assessing method applicability and environmental interpretation (see Section 5).

5 Discussion

5.1 *Comparative analysis of the results of GSCS methods*

Our comparative analysis of core GT-06 reveals that while STD, EMM, and PCA exhibit broad consistencies in identifying primary grain-size populations, their capability to resolve subtle secondary components differs significantly. This contrasts with results from simpler sedimentary settings (e.g., core YJ; Huang, 2018) where methods often yielded high consistency (r^2 > 0.9), but echoes findings from heterogeneous environments like ODP 1146 (Wan et al., 2007), where method-dependent discrepancies (e.g., 2 components by STD vs. 3 by EMM) were pronounced. Consequently, in the mixed-signal setting of the Zhongnan Seamount, the choice of GSCS technique is critical for accurately decoupling volcanic and turbidity signals from the background hemipelagic sedimentation.

5.1.1 *Consistency and discrepancies among GSCS methods*

STD vs. EMM：S1 (2.8–4.6 μm), S2 (58.9–86.3 μm), and S3 (309.5–453.9 μm) exhibit strong consistency with EM1, EM3, and EM4, respectively (Fig. 7), confirming that both methods reliably capture the major sedimentary signals. A key discrepancy is that EM2 (27.4–45.6 μm) is detectable by EMM but undetectable via STD. This difference arises from the partial overlap between EM2 and EM3 on the grain-size distribution curve, where both components jointly form a single broad peak. When such overlap occurs, the component with greater inter-sample variability (EM3) dominates the combined variance, shifting the overall STD peak toward the EM3 range. Moreover, EM2 exhibits a broader and flatter modal shape, which disperses its variance across multiple grain-size bins, whereas EM3's sharper peak concentrates variance into fewer bins (Fig. 3). Consequently, the STD method emphasizes the sharper, higher-variance EM3 mode and fails to resolve the overlapping EM2 peak.

EMM vs. PCA：F1 (0.4–1.5 μm), F4 (98.1–143.9 μm),

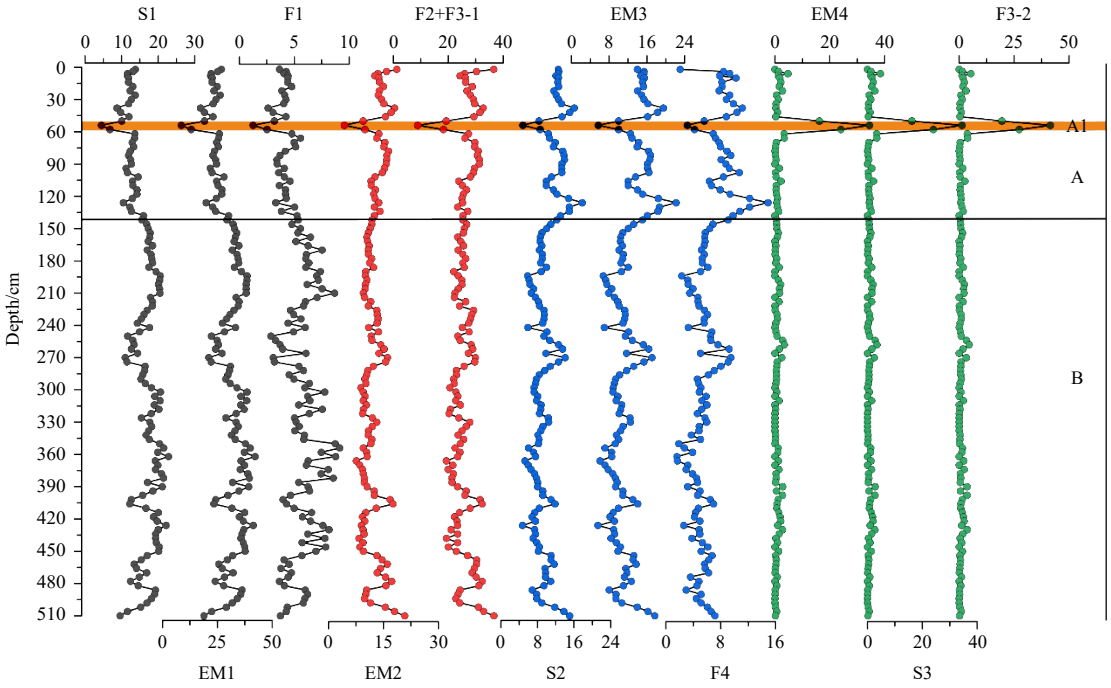

Fig. 7. Variation of components separated by three grain-size separation methods with depth in core GT-06.

F3-2 (309.5–515.8 μm) align with EM1, EM3, EM4 in grain-size range and depth trends (Fig. 7). F2 (27.4–51.8 μm) and F3-1 (8.7–14.5 μm) overlap with EM2's dominant range (27.4–45.6 μm), further validating EM2's authenticity. PCA's F3 (dual ranges: 8.7–14.5 μm and 309.5–515.8 μm) illustrates its variance based grouping. This statistical feature couples low energy fine and high energy coarse signals, rather than continuous sedimentary processes.

5.1.2 *Cross-method validation*

STD-PCA validation confirms further consistency: S1 correlates strongly with F1 (r^2 = 0.81, p < 0.01; Fig. 7), despite F1's main range (0.4–1.5 μm) not explicitly including S1 (2.8–4.6 μm). Analysis of factor loadings (Fig. 4) clarifies this relationship: grain-sizes within the S1 interval exhibit high loadings on Factor F1 (0.98) while showing negligible loadings on other factors (<0.43). This indicates that S1 and F1 represent the same dynamical population controlled by the same depositional mechanism, despite the slight offset in their calculated peak ranges.

Similarly, the other STD-identified intervals also align with specific PCA components: S2 corresponds to the variation of F4, and S3 matches the coarse fraction of F3-2, as detailed in Table 1.

Notably, no STD-identified fractions are integrated into adjacent PCA components (e.g., r^2 = 0.02 between F1 and F3-1, p > 0.05), ruling out signal overlap. Overall, STD- and PCA-derived sensitive signals show consistent depth trends (Fig. 7), demonstrating good methodological compatibility (Chen et al., 2013; He et al., 2015).

5.1.3 *Implications for method selection in complex deep-sea settings*

Table 1 summarizes the comparative performance of the three methods and provids key insights for tectonically active deep-sea basins. Our findings suggest that while STD is a simple tool for large-scale screening and major event identification (e.g., S3), its utility is limited by the subjectivity involved in defining grain-size boundaries and its tendency to overlook low-abundance components (e.g., EM2). PCA effectively extracts variance-based signals but may statistically group distinct sedimentary processes (e.g., F3's dual ranges). In contrast, EMM demonstrates superior capability in resolving complex mixed signals by accurately determining end-member numbers and isolating subtle components, albeit with higher computational demands.

5.2 *Environmental interpretation of GSCS components*

To robustly interpret the sedimentary dynamics of the Zhongnan Seamount, we integrate the GSCS-derived components with site-specific proxies (MS, LOI). We also validate them against comparative data from other marginal seas (Table S2). This approach balances site-specific insights with methodological generality. Based on the comparative analysis in Section 5.1, we primarily utilize the EMM results (EM1–EM4) as the framework for environmental interpretation, as this method proved most effective in disentangling the specific monsoon, volcanic, and turbidity signals preserved in core GT-06.

A synthesis of findings from the studies listed in Table S2 reveals the global consistency of clay-sized components as fluvial/monsoon proxies and coarse sand as turbidite indicators. However, this comparison highlights the site-specific uniqueness of Zhongnan Seamount, where the 27.4–51.8 μm fraction is of volcanic origin, distinct from other regions where similar fractions typically reflect aeolian or fluvial inputs. Based on these comparative insights and site-specific proxies (Figs 2 and 8), the four GSCS-derived components in core GT-06 are linked to distinct sedimentary processes.

(1) Clay-sized component (0.4–6.7 μm: F1/EM1/S1)

Although this component exhibits statistically significant but weak negative correlations with LOI550 (r = −0.265, p < 0.01) and MS (r = −0.283, p < 0.01), its primary identification relies on its grain-size characteristics which are consistent with terrigenous clay. The weak correlations likely reflect the complexity of deep-sea sedimentation where multiple sources mix, diluting simple linear relationships. However, comparative data from SCS cores (e.g., PC338, Li et al., 2019) show that clay in the range of 0.4 μm to 6.7 μm reflects summer monsoon driven fluvial input. This aligns with the clay range in core GT-06, indicating that fine terrigenous particles were transported by the Red/Zhujiang Rivers (Cai et al., 2024; Zeng et al., 2025). Notably, S1 (2.8–4.6 μm) is partially captured by F1 (0.4–1.5 μm) in PCA (loading = 0.98, Fig. 4), confirming shared monsoon-driven dynamics across methods (Section 5.1).

Our interpretation of EM1 as a monsoon-driven terrigenous clay component aligns with the geochemical and mineralogical evidence from Zeng et al. (2025), who studied core GT05 from the northern slope of the SCS. These features were interpreted as reflecting mixed continental and island-arc sources, modulated by monsoon-controlled

Table 1. Comparison of grain-size sensitive components extracted from core GT-06 sediments

PCA/μm	EMM/μm	STD/μm
F1(0.4−1.5)	EM1(2.1−6.7)	S1(2.8−4.6)
F2(27.4−51.8); F3-1(8.7−14.5)	EM2(27.4−45.6)	−
F4(98.1−143.9)	EM3(58.9−98.1)	S2(58.9−86.3)
F3-2(309.5−515.8)	EM4(309.5−453.9)	S3(309.5−453.9)

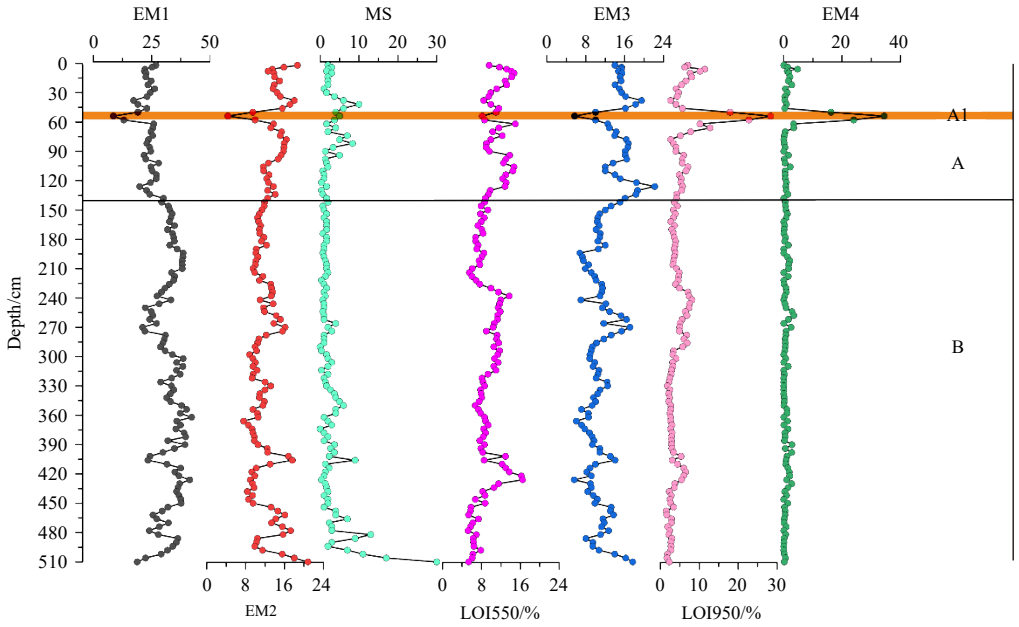

Fig. 8. Core GT-06 contents for the four end-member components and LOI and MS.

sediment supply, thereby supporting our inference of EM1's origin.

(2) Volcanic silt component (8.7–51.8 μm: F2/F3-1/EM2)

Unique to EMM/PCA (undetected by STD; Section 4.2.2), this component correlates positively with MS (r = 0.456, p < 0.01), where high MS indicates abundant magnetic minerals in volcanic detritus (Chen et al., 2007; Cai et al., 2022; Shin et al., 2020). EM2 (27.4–45.6 μm) has a modal peak at 35.3 μm, matching volcanic glass fractions in SCS volcanic event layers (e.g., Chen et al., 2007). Its vertical distribution is non-uniform: abundance reaches 14% in the 450–510 cm interval (mean MS = 8.67, vs. core mean = 2.93), further confirming intermittent volcanic input. In contrast to Mediterranean cores, where similar grain-size fractions reflect aeolian input (Beuscher et al., 2017; Hamann et al., 2008), the EM2 component in core GT-06 is associated with turbidity transport triggered by submarine eruptions, which is consistent with the seamount's proximity to the Luzon Arc (tectonically active; Chen et al., 2007).

Zeng et al. (2025) likewise recognize volcanic-derived influence in GT05 and interpret the parent rocks of some sediment fractions as andesitic to felsic volcanic types within a continental-island-arc tectonic setting, and they identify provenance shifts involving Luzon and other island sources. These independent geochemical fingerprints from the northern slope support our identification of EM2 as containing a substantial volcanic/supra-crustal component, although the exact volcanic facies and depositional conditions differ between the shallower northern slope (GT05) and our deeper southern-flank GT-06 site.

(3) Biogenic coarse silt component (58.9–143.9 μm: F4/EM3/S2)

EM3 (58.9–98.1 μm) represents the coarse silt to fine sand fraction in core GT-06. Crucially, this specific grain-size range aligns with the "second component" (modal size ~40–70 μm) identified by Wang and Chen (2013) in central SCS surface sediments. They explicitly demonstrated that while this fraction contains abundant foraminifera in shallower slope waters, it consists primarily of diatoms in deep basin areas below the CCD (~3 400–3 700 m; Liu et al., 2022a) due to the dissolution of calcareous tests.

This mechanism perfectly explains the characteristics of EM3 in core GT-06 (3 837 m water depth): While EM3 shows a statistically significant but weak positive correlation with LOI550 (r = 0.207, p < 0.05), implying a minor organic association, it shows no correlation with LOI950 (r = 0.003, p > 0.05), indicating a negligible contribution from carbonate fragments.

Therefore, supported by both regional sedimentary patterns (Wang and Chen, 2013) and site-specific geochemical evidence, EM3 is interpreted as a siliceous biogenic component dominated by diatom fragments.

(4) Turbidity current coarse sand component (309.5–515.8 μm: F3-2/EM4/S3)

EM4 (309.5–453.9 μm) is the coarsest end-member (average abundance 1.38%) and exhibits a sharp peak at 50–58 cm (Subunit A1, abundance = 24.88%, vs. core mean = 1.38%), coinciding with LOI950 = 28.34% (Section 4.1), and far exceeding the central SCS basin average (<4%, Cai et al., 2022). This component shows a strong positive correlation with LOI950 (r = 0.861, p < 0.01). This high carbonate content (unusual for CCD-below settings) confirms rapid burial of calcareous bioclasts by high-energy turbidity currents (no time for dissolution). EM4's grain-size range and poor sorting (σ_1 = 2.61) match seamount collapse-induced turbidity deposits (Zhang et al., 2003; Xiao et al., 2021). Unlike climate-driven turbid-

ity currents (e.g., typhoon-induced), GT-06's distance from fluvial sources means EM4 specifically records tectonically triggered seamount collapse: a unique signal of the central SCS's tectonic activity.

The above component-specific interpretations provide a foundation for further exploring end-member interactions and the unique sedimentary dynamics of Zhongnan Seamount, as discussed in Section 5.2.2.

5.2.1 *Comparative validation*

Table S2 summarizes GSCS component interpretations across marginal seas, highlighting two key insights that validate GT-06's results while emphasizing its uniqueness.

Methodological consistency across basins: Clay-sized components (0.4–10 μm) consistently reflect fluvial/monsoon input, and coarse sand (>300 μm) components consistently indicate high-energy events (e.g., turbidity currents) in the SCS, East China Sea, and Mediterranean. This consistency validates that GT-06's core interpretations (EM1 corresponds to monsoon clay, EM4 corresponds to turbidity sand) are not site-specific anomalies but align with global marginal sea patterns.

Site-specific uniqueness of GT-06: Unlike other SCS/Mediterranean cores (where 27.4–51.8 μm components reflect aeolian or fluvial input), the 27.4 μm to 51.8 μm component (EM2) in core GT-06 is of volcanic origin. This underscores tectonic and volcanic in fluence the central SCS's. This difference highlights the need for site-adapted GSCS interpretations, rather than direct extrapolation from other regions.

Notably, single-method GSCS risks misinterpretation (e.g., STD omitting EM2 in GT-06). For complex deep-sea settings (e.g., seamount flanks with mixed signals), we recommend EMM as the core method that resolves low abundance components, with cross validation by STD and PCA. This workflow, validated in core GT-06, balances resolution and reliability.

5.2.2 *End-member interaction and site-specific significance*

Building on the single-end-member environmental links established in Section 5.2, we now focus on their coupling relationships and site-specific significance in the central SCS, and address the core theme of this paper: monsoon volcanic interactions and turbidity current events.

(1) Coupling between volcanic input and turbidity currents

A critical observation from GT-06 is the temporal relationship between EM2 (volcanic silt) and EM4 (turbidity sand): EM2 high-abundance layers (450–510 cm) stratigraphically underlie EM4 peaks (380–400 cm). The intervening ~50 cm interval represents background sedimentation, with its duration dependent on accumulation rates. This stratigraphic sequence implies that submarine volcanic activity may have primed Zhongnan Seamount's slopes. Specifically, the destabilization of the seamount slopes is likely linked to seismic activity associated with submarine volcanism (Sun et al., 2021), where tectonic tremors or eruptive vibrations weaken the shear strength of sediments on the seamount's flanks (Masson et al., 2002). These seismic events act as triggers for landslides or slope failures, subsequently initiating turbidity currents capable of transporting large volumes of coarse calcareous sediment (EM4) (Zhu et al., 2019). This type of "volcanic–turbidity coupling" has rarely been reported in other SCS cores (e.g., PC338, Li et al., 2019, recovered from a deep-water slope setting and lacking EM2, the volcanic silt) and reflects the unique tectonic setting of Zhongnan Seamount (proximal to the Luzon Arc).

(2) Monsoon-driven controls on terrigenous and biogenic end-members

EM1 (terrigenous clay) and EM3 (coarse silt component) show a significant negative correlation (r = –0.71, p < 0.01), reflecting a competitive relationship between terrigenous input and pelagic biogenic processes in the deep central SCS. This inverse coupling is primarily driven by monsoon forcing: during periods of intensified summer monsoon, enhanced river discharge and sediment load increase the flux of fine-grained terrigenous clay (higher EM1 abundance). The resulting rise in water turbidity and sedimentation rate not only dilutes the relative proportion of biogenic particles but also suppresses siliceous primary productivity through light limitation, leading to a decrease in EM3 abundance. In contrast, during weaker summer monsoon phases, reduced terrigenous input and enhanced vertical stratification of the water column favor the proliferation and preservation of siliceous organisms such as diatoms, resulting in relatively higher EM3 abundance. In addition, the seamount setting may enhance water-column mixing and sediment resuspension through internal tides and bottom currents, thereby influencing the preservation efficiency of biogenic signals

(3) Comparison with other SCS seamounts

Zhongnan Seamount's GSCS results stand out when compared to other SCS seamounts:

Volcanic signal: Unlike Huangyan Seamount (Cai et al., 2022), where EM2 is weak and transitional, Zhongnan Seamount's EM2 confirms its function as a volcanic archive for the central SCS. It lies close to the Luzon Arc yet sufficiently distant to avoid direct tephra burial, and thus represents a rare archive for recording monsoon, volcanic and turbidity interactions in the central SCS.

Turbidity signal: EM4's high carbonate content (28.34% LOI950) distinguishes it from most surface sediments along the Huangyan–Zhenbei seamount chain in the northern and central SCS (LOI < 15%, Cai et al., 2022), while it is consistent with locally elevated LOI values observed at the southern margin of the Southeast Sub-basin (14%–24%, Cai et al., 2022). This suggests that the high carbonate content at Zhongnan Seamount reflects faster burial under CCD conditions, potentially enhanced by

flank topographic highstand that slows bottom currents and reduces dissolution (Liu et al., 2022b).

Collectively, these site-specific differences reinforce that Zhongnan Seamount is an ideal natural laboratory for resolving monsoon-volcanic-turbidity interactions, thereby filling a critical gap in SCS deep-sea sedimentary research.

6 Conclusions and perspectives

Herein, we systematically compared three GSCS methods, namely STD, EMM and PCA, using sediment core GT-06 recovered from the Zhongnan Seamount in the central South China Sea. By integrating multi-proxy validation (MS, LOI), we clarify the methodological applicability and environmental significance of grain-size components, with key conclusions as follows:

(1) Methodological insights for complex deep-sea settings

The three GSCS methods show high compatibility in identifying major sedimentary signals but differ in resolution:

STD: Efficient for large-scale rapid screening of dominant sensitive intervals (e.g., S1–S3);

PCA: Effective for dimensionality reduction and extracting major environmental signals (cumulative variance >98.2%), but may generate redundant correlated components (e.g., F3's dual grain-size ranges) that complicate independent process interpretations;

EMM: Offers the highest accuracy in isolating geologically meaningful end-members (e.g., volcanic EM2, turbidity EM4) via reconstruction variance (>99.6%) and angular deviation (<5%), albeit with higher computational cost.

We propose a multi-method GSCS workflow tailored for tectonically active deep-sea basins: EMM serves as the core separation method, PCA is used for cross-validation, and STD provides preliminary large-dataset screening.

(2) End-member-based proxy system for monsoon-volcanic-turbidity interactions

Four EMM-derived end-members (EM1–EM4) form a site-specific environmental proxy system for the Zhongnan Seamount:

EM1 (2.1–6.7 μm): Terrigenous clay transported by the Red/Zhujiang Rivers, indicating East Asian summer monsoon (EASM) intensity;

EM2 (27.4–45.6 μm): Volcanic detritus (positive correlation with MS), reflecting Quaternary submarine volcanic activity in the central SCS;

EM3 (58.9–98.1 μm): Siliceous biogenic debris (positive correlation with LOI550), reflecting monsoon-modulated siliceous productivity and preservation below the CCD;

EM4 (309.5–453.9 μm): Calcareous bioclasts in turbidites (strong correlation with LOI950), signaling seamount collapse-induced high-energy events.

This study validates the use of GSCS methods in the unique tectonic setting of the central SCS. However, several limitations still exist. For instance, the temporal framework of component variations remains unclear because of the absence of U/Th dating or AMS 14C analysis, which restricts correlations with global climate events such as Dansgaard-Oeschger cycles. Future work will focus on two key goals: first, incorporate U/Th dating of carbonate-rich layers (e.g., A1) to establish a high-resolution chronology; second, employ SEM-EDS or EPMA analyses to geochemically characterize the amorphous volcanic glass fraction in EM2. These efforts will address current limitations and enhance regional paleoenvironmental interpretations.

Acknowledgements

We are grateful to Kedong Yin, Wei Xie, and Mengyuan Wang from the Southern Marine Science and Engineering Guangdong Laboratory (Zhuhai) for providing the samples.

References

Beuscher S, Krüger S, Ehrmann W, et al. 2017. End-member modelling as a tool for climate reconstruction-an Eastern Mediterranean case study. PLoS One, 12(9): e0185136

Boulay S, Colin C, Trentesaux A, et al. 2003. Mineralogy and sedimentology of Pleistocene sediment in the South China Sea (ODP Site 1144). In: Proceedings of the Ocean Drilling Program: Scientific Results. College Station, USA: Ocean Drilling Program, 1–21

Boulay S, Colin C, Trentesaux A, et al. 2007. Sedimentary responses to the Pleistocene climatic variations recorded in the South China Sea. Quaternary Research, 68(1): 162–172, doi: 10.1016/j.yqres.2007.03.004

Cai Guanqiang, Li Shun, Zhao Li, et al. 2018. Geochemical characteristics of surface sediments from the middle deep-sea basin of South China Sea. Marine Geology & Quaternary Geology (in Chinese), 38(5): 90–101

Cai Zhourong, Wang Xiaoxiang, Zhong Lifeng, et al. 2024. The sources and transport model of deep-sea sediment in the Southwest Sub-basin of the South China Sea. Frontiers in Marine Science, 11: 1440886

Cai Guanqiang, Xu Yonghang, Zhong Hexian, et al. 2022. Terrigenous and volcanogenic contribution to the deep basin of the South China Sea: evidence from trace elements and Sr-Nd isotopes. Marine Geology, 448: 106811, doi: 10.1016/j.margeo.2022.106811

Chen Qiao, Liu Dongyan, Chen Yingjun, et al. 2013. Comparative analysis of grade-standard deviation method and factors analysis method for environmental sensitive factor analysis. Earth and Environment (in Chinese), 41(3): 319–325

Chen Junjin, Wu Shiguo, Liu Shiqiao, et al. 2022. Sedimentary dynamics in the distal margin around isolated carbonate

platforms of the Northern South China Sea. Frontiers in Earth Science, 10: 884921

Chen Guocheng, Zheng Hongbo, Li Jianru, et al. 2007. Sedimentary records of volcanic activities in the South China Sea over the past 480 ka. Marine Geology & Quaternary Geology (in Chinese), 27(4): 69–76

Flemming B W. 2007. The influence of grain-size analysis methods and sediment mixing on curve shapes and textural parameters: implications for sediment trend analysis. Sedimentary Geology, 202(3): 425–435

Folk R L, Ward W C. 1957. A Study in the Significance of Grain-Size Parameters. Journal of Sedimentary Petrology, 27: 3–26, doi: 10.1306/74D70646-2B21-11D7-8648000102C1865D

Hamann Y, Ehrmann W, Schmiedl G, et al. 2008. Sedimentation processes in the Eastern Mediterranean Sea during the Late Glacial and Holocene revealed by end-member modelling of the terrigenous fraction in marine sediments. Marine Geology, 248(1–2): 97–114

Hao Rongrong, Yang Yihong, Zhu Longhai, et al. 2023. Application of environmentally sensitive factors in bay sedimentary environments. Acta Sedimentologica Sinica (in Chinese), 41(3): 763–777

He Jishan, Liang Xing, Li Jing, et al. 2015. Environmentally sensitive grain-size extraction of deep hole sediment from Tianjin Coastal Plain and its significance. Earth Science (in Chinese), 40(7): 1215–1225

Howe J A, Stoker M S, Masson D G, et al. 2006. Seabed morphology and the bottom-current pathways around Rosemary Bank seamount, northern Rockall Trough, North Atlantic. Marine and Petroleum Geology, 23(2): 165–181

Huang Chao. 2018. Holocene climate change and human activity from an archive of continental shelf sediments in the northern South China Sea (in Chinese)[dissertation]. Guangzhou: Guangzhou Institute of Geochemistry, Chinese Academy of Sciences

Jiang Xuejiao, Wang Kunshan, Dong Zhi, et al. 2023. Sea ice variations in the northern Okhotsk Sea shelf since the Last Glacial Maximum. Haiyang Xuebao (in Chinese), 45(5): 1–13

Li Mingkun, Ouyang Tingping, Tian Chengjing, et al. 2019. Sedimentary responses to the East Asian monsoon and sea level variations recorded in the northern South China Sea over the past 36 kyr. Journal of Asian Earth Sciences, 171: 213–224

Lin Jinhui, Zou Jianjun, Shi Xuefa, et al. 2023. Rapid changes in sedimentary environment on the northern slope of the Bering Sea during the early Holocene. Haiyang Xuebao (in Chinese), 45(11): 45–61

Liu Shiqiao, Chen Wanli, Zhang Muhui, et al. 2022a. Distribution of planktonic foraminifera in surface sediments and its environmental implication in the Zhongsha waters, South China Sea. Marine Geology Frontiers (in Chinese), 38(9): 13–25

Liu Jianliang, Liu Keyu, Salles T, et al. 2022b. Factors controlling carbonate slope failures: insight from stratigraphic forward modelling. Earth-Science Reviews, 232: 104108

Masson D G, Watts A B, Gee M J R, et al. 2002. Slope failures on the flanks of the western Canary Islands. Earth-Science Reviews, 57(1–2): 1–35

Paterson G A, Heslop D. 2015. New methods for unmixing sediment grain size data. Geochemistry, Geophysics, Geosystems, 16(12): 4494–4506

Prins M A, Postma G, Weltje G J. 2000. Controls on terrigenous sediment supply to the Arabian Sea during the Late Quaternary: the Makran continental slope. Marine Geology, 169(3–4): 351–371

Shin J Y, Kim W, Hyeong K. 2020. High potency of volcanic contribution to the ~400 kyr sedimentary magnetic record in the Northwest Pacific. Frontiers in Earth Science, 8: 300

Sun Qiliang, Xie Xinong, Wu Shiguo. 2021. Submarine landslides in the northern South China Sea: characteristics, geohazard evaluation and perspectives. Earth Science Frontiers (in Chinese), 28(2): 258–270

Tian Xu, Xu Fangjian, Xu Wei, et al. 2015. 4 400 a East Asian monsoon record from sediments in the continental shelf of the northern South China Sea. Marine Sciences (in Chinese), 39(9): 62–68

Wan Shiming, Li Anchun, Stuut J B W, et al. 2007. Grain-size records at ODP site 1146 from the northern South China sea: implications on the east Asian monsoon evolution since 20 Ma. Science in China Series D: Earth Sciences, 50(10): 1536–1547

Wang Pinxian. 2020. Exploring the deep sea processes in the South China Sea. Science & Technology Review (in Chinese), 38(18): 6–20

Wang Weiguo, Chen Jian. 2013. Characters of grain-size populations of sediments in central South China Sea. Journal of Applied Oceanography (in Chinese), 32(3): 295–304

Wang Jiahao, Hu Xiumian, Jiang Jingxin, et al. 2024. High-resolution reconstruction of carbonate compensation depth in the South China Sea since 27 Ma. Earth Science Frontiers, 51(1): 500–510

Weltje G J. 1997. End-member modeling of compositional data: numerical-statistical algorithms for solving the explicit mixing problem. Mathematical Geology, 29(4): 503–549

Weltje G J, Prins M A. 2003. Muddled or mixed? Inferring palaeoclimate from size distributions of deep-sea clastics. Sedimentary Geology, 162(1–2): 39–62

Xiao Qianwen, Feng Xiuli, Miao Xiaoming. 2021. Turbidity deposits and their provenance: evidence from core SH37 in Shenhu area of the South China Sea. Marine Geology & Quaternary Geology (in Chinese), 41(5): 101–111

Yan Quanshu, Shi Xuefa, Castillo P R. 2014. The late Mesozoic-Cenozoic tectonic evolution of the South China Sea: a petrologic perspective. Journal of Asian Earth Sciences, 85: 178–201

Yang Wenguang, Zheng Hongbo, Wang Ke, et al. 2007. Sedimentary characteristic of terrigenous clast of site MD05–2905 in the northeastern part of South China Sea after 36ka and evolution of East Asian Monsoon. Advances in

Earth Sciences (in Chinese), 22(10): 1012–1018

Yi Liang, Yu Hongjun, Ortiz J D, et al. 2012. Late Quaternary linkage of sedimentary records to three astronomical rhythms and the Asian monsoon, inferred from a coastal borehole in the south Bohai Sea, China. Palaeogeography, Palaeoclimatology, Palaeoecology, 329–330: 101–117

Yu Shiyong, Colman S M, Li Linxiong. 2016. BEMMA: a hierarchical Bayesian end-member modeling analysis of sediment grain-size distributions. Mathematical Geosciences, 48(6): 723–741

Yue Yuanfu, Tang Lichao, Yu Kefu, et al. 2024. Coral records of Mid-Holocene sea-level highstands and climate responses in the northern South China Sea. Acta Oceanologica Sinica, 43(2): 43–57, doi: 10.1007/s13131-023-2264-9

Zeng Letian, Wang Ce, Su Ming, et al. 2025. Provenance of sediments in the Zhongnan Seamount, South China Sea since MIS 3: insights from clay minerals and geochemical signatures. Quaternary Science Reviews, 369: 109585

Zhang Lanlan, Wang Rujian, Chen Muhong, et al. 2015. Biogenic silica in surface sediments of the South China Sea: controlling factors and paleoenvironmental implications. Deep-Sea Research Part II: Topical Studies in Oceanography, 122: 142–152

Zhang Weiyan, Zhang Fuyuan, Zhang Xiaoyu. 2003. Characteristics of turbidity deposits from sediment cores in eastern South China Sea. Journal of Tropical Oceanography (in Chinese), 22(3): 36–43

Zhao Song, Chang Fengming, Li Tiegang, et al. 2017. The application of grain-size end-member algorithm to paleoenvironmental reconstruction on inner shelf of East China Sea. Marine Geology & Quaternary Geology (in Chinese), 37(3): 187–196

Zhu Chaoqi, Cheng Sheng, Li Qingping, et al. 2019. Giant submarine landslide in the South China Sea: evidence, causes, and implications. Journal of Marine Science and Engineering, 7(5): 152

Supplementary information:

Table S1. Principal component analysis (PCA) results for core GT-06.

Table S2. Application of GSCS methods in sediment cores from the marginal seas of China, as well as other regions.

The supplementary information is available online at https://doi.org/10.1007/s13131-025-2587-9 and http://www.aosocean.com/. The supplementary information is published as submitted, without typesetting or editing. The responsibility for scientific accuracy and content remains entirely with the authors.